Research Article Vol. 30, No. 1 / 3 Jan 2022 / Optics Express 403
Optics EXPRESS

Maskless Fourier transform holography

KAHRAMAN KESKINBORA,[1,2,3,4] ABRAHAM L. LEVITAN,[2] AND RICCARDO COMIN[2,5]

[1]Max Planck Institute for Intelligent Systems, Heisenbergstrasse 3, 70569 Stuttgart, Germany
[2]Massachusetts Institute of Technology, 77 Mass Avenue, Cambridge, MA 02139, USA
[3]Harvard University, John A. Paulson School of Applied Sciences, Center for Integrated Quantum Materials, 19 Oxford Street, Cambridge, MA 02138, USA
[4]kahraman@mit.edu
[5]rcomin@mit.edu

Abstract: Fourier transform holography is a lensless imaging technique that retrieves an object's exit-wave function with high fidelity. It has been used to study nanoscale phenomena and spatio-temporal dynamics in solids, with sensitivity to the phase component of electronic and magnetic textures. However, the method requires an invasive and labor-intensive nanopatterning of a holography mask directly onto the sample, which can alter the sample properties, forces a fixed field-of-view, and leads to a low signal-to-noise ratio at high resolution. In this work, we propose using wavefront-shaping diffractive optics to create a structured probe with full control of its phase at the sample plane, circumventing the need for a mask. We demonstrate *in silico* that the method can image nanostructures and magnetic textures and validate our approach with a visible light-based experiment. The method enables investigation of a plethora of phenomena at the nanoscale including magnetic and electronic phase coexistence in solids, with further uses in soft and biological matter research.

1. Introduction

The phase of the exit-wave leaving a coherently illuminated sample contains critical information relating to the internal structure of the sample. However, this information is lost during detection. This so-called missing-phase problem is ubiquitous in optical, electron, and X-ray microscopy. It has motivated a rich variety of imaging techniques using both photons and electrons to recover the complex sample exit wave from recorded far-field intensity patterns. These methods include in-line [1], off-axis [2], and hybrid holography schemes [3], as well as coherent diffractive imaging (CDI) and ptychography approaches [4–11] based on iterative reconstruction algorithms [12,13]. These phase-sensitive imaging methods are well-positioned to reap the scientific benefits of technical advances in high-coherence X-ray sources such as diffraction-limited synchrotrons and free-electron lasers [14–17] for ultra-high time resolution imaging at the nano- and mesoscale.

X-ray Fourier transform holography (FTH) is one of the most successful of these approaches in X-ray phase-contrast imaging [18,19]. In the FTH approach, a holography mask composed of a micron-sized sample aperture and a nanometer-sized reference aperture is fabricated directly onto the sample. The major advantage of FTH is the simplicity of the reconstruction method, implemented using a single Fourier transform. It is also compatible with single-shot imaging. However, this comes at the steep price of a fixed, preselected sample region of interest, inefficient utilization of the total incident photon flux, and labor-intensive sample preparation.

Several approaches have been proposed to improve on these aspects of FTH [19–23]. For instance, to extend the field of view beyond the prefabricated sample window, Guehrs *et al.* separated the holography mask from the sample. Hessing *et al.* were able to overcome the field of view limitations by using a separate mask on a different stage close to the sample [21]. Geilhufe *et al.* utilized a Fresnel zone plate (FZP) instead of a reference aperture to overcome the diminishing

#444455 https://doi.org/10.1364/OE.444455
Journal © 2022 Received 27 Sep 2021; revised 9 Dec 2021; accepted 13 Dec 2021; published 21 Dec 2021

Optics EXPRESS

light transmission through a nano-sized reference hole [22] and enhance the signal-to-noise ratio. However, while the latter improves the signal rate, the region of interest remains fixed. In an earlier implementation of X-ray FTH, McNulty *et al.* used the 0^{th} order light transmitting through an FZP to illuminate the sample while the focus of the FZP provided a reference point source [19].

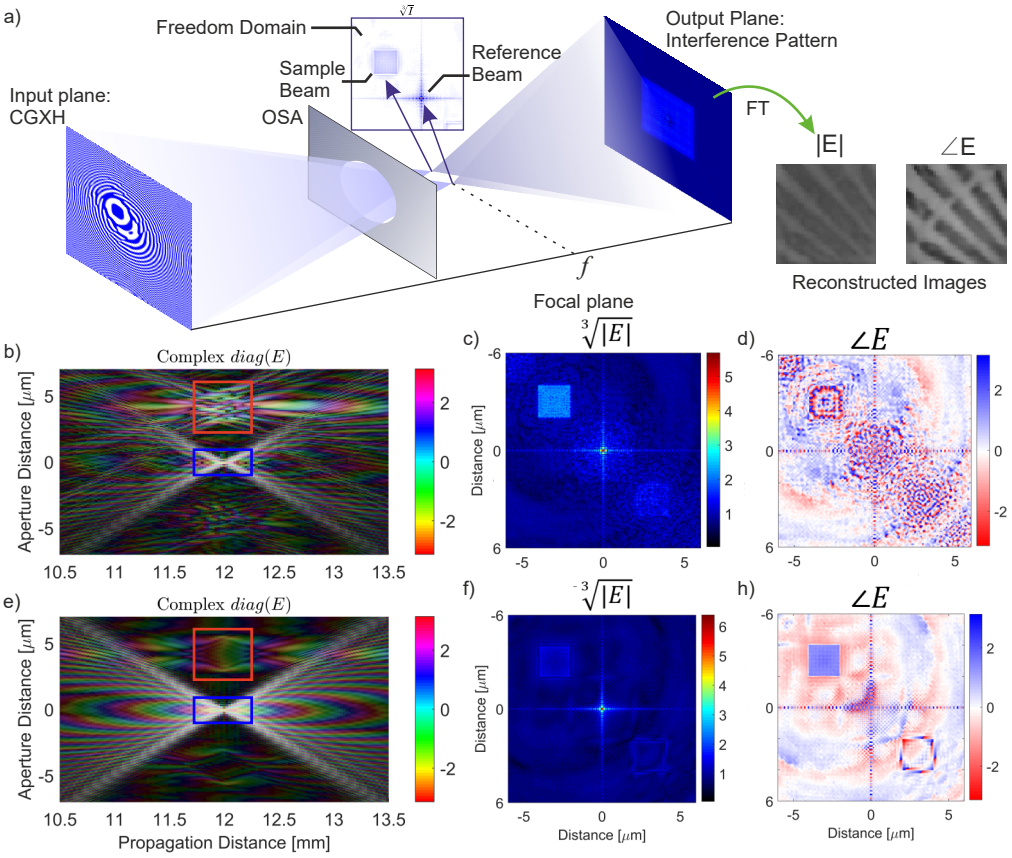

Fig. 1. Schematic description of the proposed experiment. a In the StIXH experiment, a computer-generated X-ray hologram is illuminated by a coherent plane wave. Two separate beams with tailored complex-amplitudes are simultaneously projected onto the sample in lieu of the transmission mask, by a computer-generated hologram. A spatial filter called an order sorting aperture eliminates the spurious diffraction orders. The sample is illuminated by structured light at the focal plane (f), and the sample beam is imprinted with sample information such as chemical, structural, electronic/magnetic properties. An area detector captures the far-field interference pattern of the sample and the reference beams. A Fourier transform of the interference pattern yields the amplitude and phase images of the sample. b A 2D diagonal slice of the complex field created by a hologram synthesized using GSA, along the propagation direction near the focal plane (12 mm). Note the scrambled phase of the sample beam and the intensity variation (marked red) in relation to the reference beam (marked blue). c, d The amplitude and phase of the structured illumination pattern of a GSA hologram at f exhibit speckle noise in the sample beam as a result of constructive and destructive interference within this region due to the random phase. e Slice of the complex field of a DC-GSA hologram at f. Notice how the sample-beam has a flat phase at the focal plane in contrast to b. f, h The amplitude and phase of DC-GSA holograms at f clearly show relatively flat phase and intensity distribution.

Optics EXPRESS

More recently, Balyan and Haroutunyan devised an FTH scheme based on a two- or three-FZP interferometer to project the object and reference beams onto a sample, again with a fixed field of view and with reduced photon efficiency due to the multiplicative impact of the zone plates' transmission rates [23]. Also recently, a method for producing structured illumination at the focal plane of a binarized X-ray optic was proposed by Marchesini and Sakdinawat [24]. Their approach depends on modifications to the amplitude and phase at the plane of a binary X-ray optic by varying the duty cycle, zone positions, harmonics, etc. to create the desired structured illumination at the focal plane. Among other imaging methods, holography is mentioned as a possible application of these optics.

Here, we lay out and describe in detail all the necessary steps for removing the dependence of off-axis X-ray holography on the hard-encoded holography mask. We combine different elements from digital holography, holographic image projection, and holographic imaging to present an imaging scheme that utilizes structured illumination instead of a mask. All aspects of the proposed FTH modality, from the synthesis of the computer-generated holograms to the computer simulations and visible light experiments of the full FTH imaging cycle are explicitly defined, clarified, and studied.

In the approach we propose here, a beam-shaping optic, synthesized using a double-constraint Gerchberg-Saxton algorithm [25], concentrates incident X-rays to form a structured illumination pattern at the sample plane. This pattern is composed of a large, uniformly illuminated sample beam and a tightly focused reference beam with a well-defined phase relationship between the two. By making use of this optic, we simultaneously address all three abovementioned challenges of the FTH method. A schematic summary of the full imaging scheme that we call Structured Illumination X-ray Holography, StIXH, is shown in Fig. 1(a). The decoupling between the holographic (virtual) mask and the sample opens new experimental possibilities that are otherwise impossible, as will be discussed later.

2. Synthesis of the computer generated holograms

Holographic image projection is an active field of research with applications in 3D displays [26], acoustic medical imaging [27], and X-ray beam shaping [24]. In many holographic image projection applications, computer-generated holograms only project the designed intensity pattern without tailoring the phase at the projection plane. The projected intensity profiles usually suffer from the so-called speckle noise caused by a random phase distribution within the field. This phase distribution is detrimental if structured illumination is to be used for holographic microscopic imaging. Numerous speckle-noise reduction methods are available in holographic image projection [28]. Optical routes for speckle suppression depend on reducing the coherence, for instance, by using diffusers [29]. However, to achieve X-ray holography using structured light, we simultaneously need tailored phase and amplitude profiles (so-called complex-amplitude control) and a high degree of coherence at the sample plane. Therefore, coherence reduction approaches cannot be applied here.

The possibility of simultaneously tailoring an amplitude and phase field has been explored in the context of digital holographic image formation to speckle noise reduction. Such approaches include using metasurfaces [30], spatial light modulators (SLMs) [31] or a modified Gerchberg-Saxton Algorithm [25,32] to control not only the amplitude but also the phase of the projected beam. These approaches that aim to tailor the phase and amplitude of the structured light are known as complex-amplitude control methods.

At X-ray wavelengths, spatial light modulators and meta-surfaces are not practical for speckle suppression using complex amplitude control. Hence, we follow a modified double-constraint [24] Gerchberg-Saxton algorithm (DC-GSA) [32] approach for synthesizing the computer-generated X-ray holograms (CGH) as binary diffractive optics. We synthesize the CGH by defining a signal domain composed of the sample and the reference beams in the probe field. Here, we tailor

Optics EXPRESS

both the amplitude and the phase of the beam. The rest of the probe field is composed of the freedom domain where the amplitude is ideally 0, and the phase is not explicitly modified by the algorithm, facilitating the convergence of the algorithm. During each iteration cycle of DC-GSA, the illumination amplitude within the signal domain is stepped toward the target amplitude while the phase is set to match the target phase. In contrast, within the freedom domain, the probe's amplitude is damped by a predefined factor without altering the phase. In the optic plane, a square mask is forced that defines the optic boundaries. The CGH that projects the desired probe field in the sample plane takes form after around 20 iterations (For a detailed explanation of the CGH synthesis scheme, see the SI Fig. S1, also see Fig. S2. for error progression.).

When the resulting CGH is illuminated with a plane wave, it forms a structured illumination pattern at the focal plane with a controlled amplitude and phase. An instance of such an experiment is depicted in Fig. 1(a). The differences in the projected light-field caustics between a conventional GSA and modified DC-GSA algorithms are presented in Figs. 1(b) through h. The complex field near the focal plane produced by a CGH synthesized using the conventional GSA exhibits a scrambled phase profile as shown in Fig. 1(b). The sample beam has abrupt intensity variations (Fig. 1(c)) due to its random phase distribution (Fig. 1(d)). In comparison, CGHs generated by DC-GSA control both the amplitude and phase of the wavefield, as shown by a diagonal slice of the propagated beam in Fig.1e. Both the amplitude (Fig. 1(f)) and the phase (Fig. 1(h)) at the focal plane are relatively flat and only exhibit low-frequency modulations.

We estimated the focusing efficiency of such a hologram made out of 280 nm thick gold layer to be about 10% at 1200 eV, which is well within the requirements of a state-of-the art X-ray microscope (See SI). The total intensity contained within the reference and the sample beam regions accounts for more than 87% of the total intensity behind the OSA in the focal plane P.

3. Imaging simulations

To explain the full cycle of an imaging experiment and demonstrate the capabilities of StIXH, we have carried out two in silico case studies involving a nanostructured test object and magnetic worm domains in synthetic samples. We conducted the simulations using empirical charge and magnetic scattering factors from the literature [33,34].

3.1. Structural Imaging

We first consider imaging simulations of a Siemens star test object with nano-sized features. The synthetic sample is a binarized SEM micrograph (Fig. 2(a)) which was assigned complex refractive index values from the CXRO database [33] at a thickness of 180 nm. The thin sample approximation was used to calculate the sample exit-wave, which (Fig. 2(b)) was then propagated 16 cm downstream to the detector plane using a scaled Fraunhofer propagator [35]. Only the intensity of the interference pattern, $I = |E(x, y)|^2$, was kept (Fig. 2(c)). The magnitude and phase of the sample exit-wave were then calculated by an FFT of the intensity and shown in Fig. 2(d) and Fig. 2(e), respectively. Both the amplitude and the phase of the exit-wave were reconstructed with fidelity to the original object. The spokes in the second ring structure of the Siemens star are clearly displayed. The projected reference spot is slightly larger than the design reference spot. Because the reconstructed image is formed by a convolution of the sample exit wave with the reference beam, the resolution of the final image is determined by the size of the reference beam spot size. It is worth noting here that the reconstruction is quite robust against detector shot noise. The reconstruction quality improves significantly above 10^1 photons/pixel, and reliable reconstructions can be achieved starting from 10^2 maximum photons/pixel in the detector plane (Fig. S3). For the following StIXH simulation, a maximum of 10^3 photons/pixel was used.

Optics EXPRESS

3.2. Magnetic Imaging

Next, we turn our attention to a data-driven simulation of a synthetic magnetic material with worm-domains (For details see SI Fig. S4). For the case of out-of-plane magnetization in a metal alloy material probed in the forward scattering direction by circularly polarized X-rays, the scattering factor simplifies [5] to $f^n \approx f_c^n + if_m^n \begin{pmatrix} i\,m_z^n & 0 \\ 0 & -i\,m_z^n \end{pmatrix} \approx f_c^n \pm if_m^n m_z^n$ for LC-to-LC (+) and RC-to-RC (-) polarization channels, where m_z is the magnetization vector, f_c', f_c'' and f_m', f_m'' are the real and complex parts of the charge and magnetic scattering factors, respectively. LC and RC stand for left and right circular polarization, respectively. For the simulations shown in Fig. 3, complete out of plane magnetization is assumed and as a result the scalar diffraction theory provides a satisfactory approximation.

In Fig. 3(a), a synthetic magnetic sample with a totally out-of-plane m_z is shown. The sample is modeled as a 50 nm thick CoFeB thin film by including measured f_c and f_m data (Fig. 3(b)). For a full history of the processing of the synthetic magnetic sample, please see SI Fig. S4. Simulated sample exit-wave is shown in Fig.3c. Image reconstruction results at three different

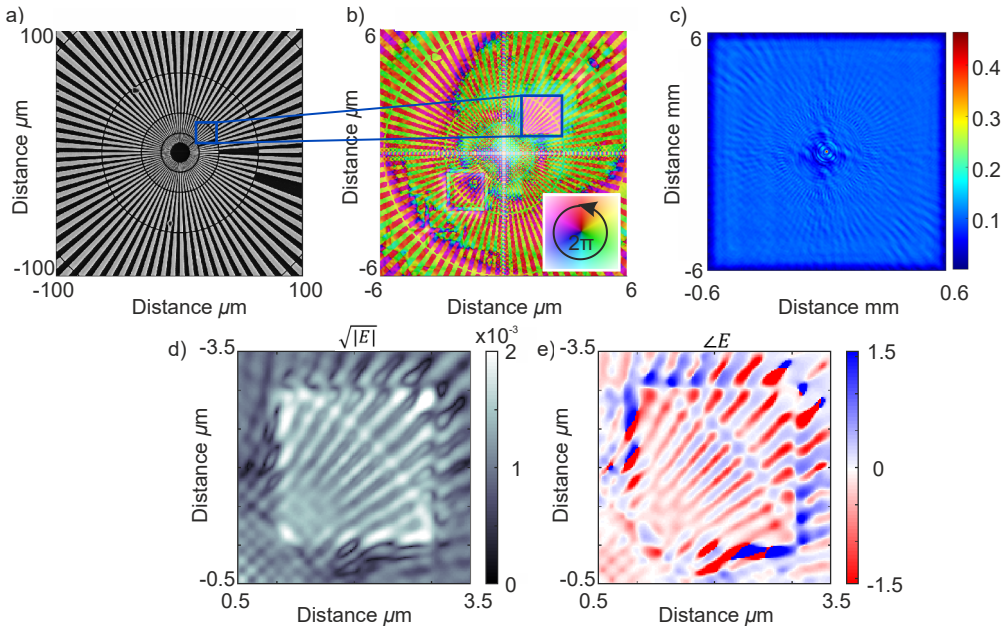

Fig. 2. Simulated StIXH imaging using synthetic data. a An SEM micrograph of the Siemens star that was used to prepare the synthetic data. The SEM image was binarized and downsampled to match the simulated support size. The overlay shows the position of the sample beam. The sample and lens gold thicknesses were taken as 180 nm and 280 nm, respectively. The refractive index data were taken from http://cxro.lbl.gov/ [33]. b The complex exit wave function shows the reference beam as the bright spot. The sample beam is imprinted with the sample information at this point. The inset shows the color-wheel, with brightness proportional to the intensity and hue to the phase. c The interference pattern as recorded 16 cm downstream from the sample plane, stretched with a cube root to exhibit its features more clearly. Only the intensity of the interference pattern is recorded at the detector plane, and the phase is lost. A scaled Fourier transform of the interference intensity distribution leads to the reconstructed amplitude (d) and phase (e) of the sample ROI illuminated by the sample-beam.

Optics EXPRESS

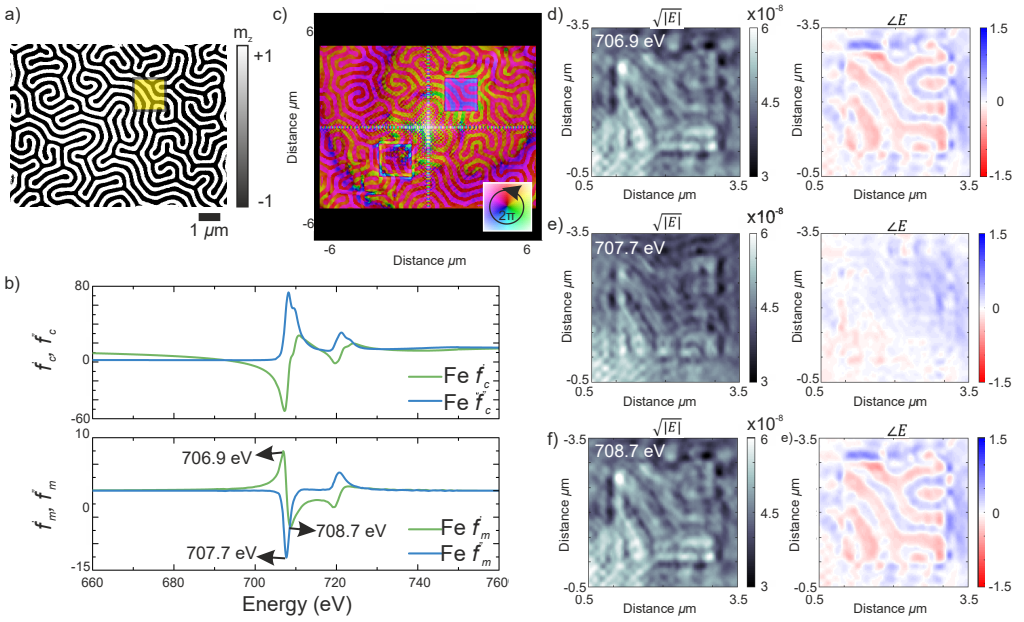

Fig. 3. Imaging simulations on magnetic worm domains using StIXH. a The domain wall structure represents the out-of-plane magnetization vectors (image source: [36]). The overlaid square shows the approximate region that is spanned by the sample beam. b The charge and magnetic structure factors for iron in CoFeB (Data courtesy of D. B. Boltje and E. Goering) [34]. c The complex exit wave function at the sample plane. Note that both the reference and the sample beam pass through the sample in this case. d, e, and f, The reconstructed square root of the amplitude and phase of the magnetic worm domain patterns at 706.9, 707.7, and 708.7 eV, respectively. CoFeB thickness was taken as 50 nm. Detector shot noise with a maximum of 1000 ph/pix.

energies are given in Figs. 3(d), (e), and f, respectively: 706.9 eV where f_m' is maximum, 707.7 eV where f_m'' is maximum and f_m'' is almost zero, and at 708.7 eV with intermediate f_m values. As expected, phase contrast is strongest where f_m' is the largest and disappears at 707.7 eV where f_m' approaches zero. Note that the sample is uniform in composition and thickness; therefore, the fc does not contribute to the contrast but results in a uniform absorption and phase shift. Further, magnetic structure factors are markedly smaller than charge scattering factors (Fig. 3(b)).

Despite significant detector shot noise, the phase and amplitude of the object exit-wave successfully capture the general features of the magnetic texture. A high spatial frequency modulation arising from the probe itself is visible, particularly in the amplitude reconstructions. In contrast, a cleaner reconstruction of the phase was achieved. Future studies will consider removing such probe-based artifacts from the image reconstruction via probe calibration by an initial ptychography scan before moving to the actual StIXH experiment or using an iterative reconstruction algorithm.

4. Holographic imaging using structured visible light

A visible light equivalent of the above-discussed X-ray imaging technique was set up to demonstrate the StIXH method experimentally. In the experiment, as shown in Fig. 4, a 635-nm laser illuminates a spatial light modulator that displays a binary CGH in half-wave mode. While it is possible to fabricate non-binary optics for X-ray energies [37–40], most high resolution diffractive X-ray optics are binary due to their relative ease of fabrication. Hence, we displayed a

Optics EXPRESS

binary representation of the hologram to more faithfully and fairly simulate the X-ray counterpart of the experiment.

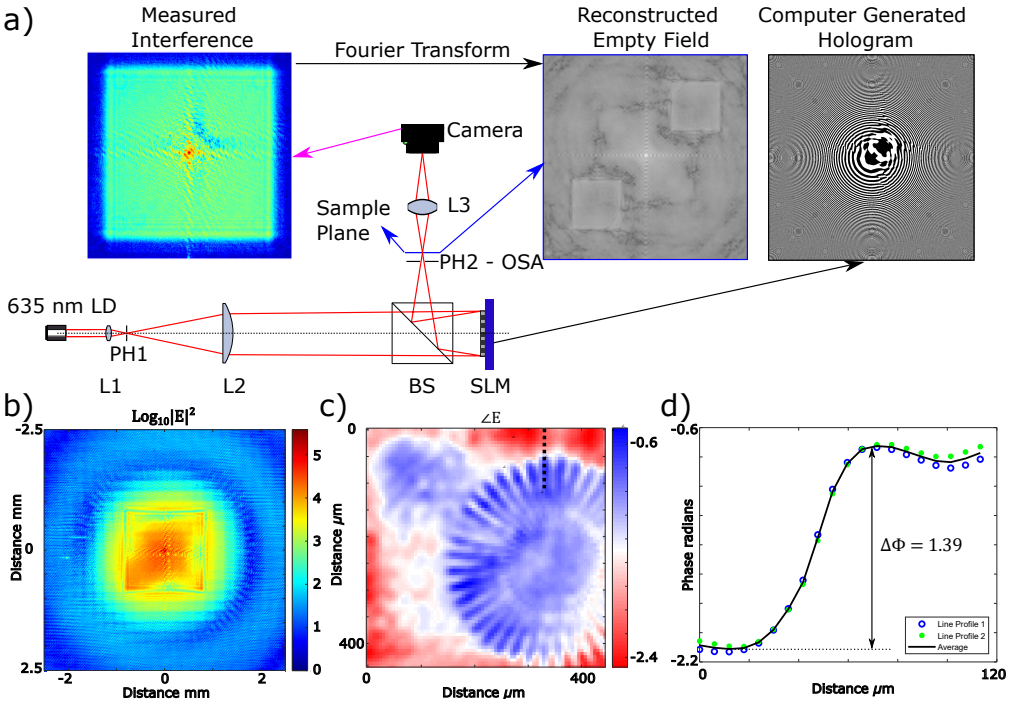

Fig. 4. Experimental demonstration of maskless FTH via structured illumination with visible light. a) Schematic of the visible light experiment. The output of a 635-nm laser is expanded and cleaned up using a Keplerian telescope combined with a pinhole. A phase-only SLM displaying the CGH forms the structure illumination pattern in the sample plane. Spurious orders are rejected using an iris. The far-field diffraction pattern is captured by a CCD using a $2f$-Fourier transform lens. b) Measured interference pattern from a Siemens star test object. c) The phase of the exit-wave of the Siemens star, reconstructed from the interference shown in b). d) Two line profiles extracted from two neighboring single-pixels wide segments in the marked section in c) cut across the featureless background and one of the spokes of the test object. The phase difference between the background and the object is about 1.39 radians corresponding to a thickness of 92 nm.

The CGH forms a structured illumination pattern with a 500-µm wide sample beam at about 30 cm downstream, where the sample was located. A $2f$-Fourier transform imaging system behind the sample mimics the far-field diffraction condition typical of X-ray holography experiments. A microscopic Siemens star-shaped phase object (QPT, Benchmark Tech, USA) was imaged using this setup. The experimental schematic and reconstructions are summarized in Fig. 4. The interference pattern generated by the computer generated hologram without a sample (Fig. 4(a)) approximates the simulation results (Fig. 2(c)). The reconstructed empty focal plane shows the conjugate fields of view. The pattern created by a sample beam that traverses the Siemens star and interferes with the reference beam in the far field is seen in Fig. 4(b). Figures 4(c) and 4(d) display the phase of the sample exit-wave and the extracted phase profile, respectively. The measured phase difference of 1.39 radians corresponds to a material thickness of 92 nm, which closely matches the specified 100 nm nominal thickness of one of the Siemens stars on the sample. Note that the phase signal is quite strong for an object with 100 nm thickness and

Optics EXPRESS

virtually no absorption at this wavelength. This demonstrates the capability of this method to image weakly absorbing phase-only objects, as discussed previously.

5. Discussion

The conventional FTH method provides excellent stability through mechanical integration of the illumination mask and sample at the cost of: (i) limiting the sample type and field of view; (ii) inefficient usage of coherent flux; and (iii) a rather labor-intensive sample preparation.

The method proposed here addresses precisely these limitations of conventional X-ray holography and provides further experimental advantages: (i) the sample and the reference beams are not defined by pre-patterned structures; (ii) The field of view is not physically anchored to a preselected region of interest, allowing free investigation of extended samples; (iii) Thanks to this separation, the proposed method is suitable not only for transmission experiments but also for a reflection geometry, enabling Bragg holography at finite momentum transfers to visualize collective phases of matter with long-range order, including charge density waves, antiferromagnetic order, topological textures (skyrmions and polar vortices), and others that are peculiar to strongly interacting electron systems; (iv) In StIXH, the relative intensity at the sample and reference beams can be freely varied; (v) StIXH uses coherent incident flux more efficiently compared to FTH, where the vast proportion of incoming photons are discarded. In addition, StIXH is compatible with single-shot, ultrafast spatiotemporal imaging of non-periodic dynamics at the nanoscale, which is not possible via stroboscopic dynamic imaging.

From a fabrication point of view, in order for the CGH optics to produce a diffraction-limited reference beam, they must meet the same quality standards as standard FZP type X-ray optics. Modern nanofabrication methods are capable of fabricating aberration-free diffraction limited X-ray holograms with a resolution limited by the outer zone width rather than the aberrations in the fabrication process. Further, modern soft X-ray coherent scattering/imaging end-stations have the capability to illuminate such optics with a single-mode high coherence incident beam. As a result, the basic requirements for the production and use of our proposed CGH optics can be met, even in the high-resolution X-ray regime.

Alongside its promises, StIXH comes with specific challenges. Most importantly, the incompatibility with a beamstop (See Fig. S5 for the impact of the beamstop on the structured illumination) is likely to be an important obstacle. As the quality of the reconstruction depends on the absence of residual light that illuminates undesired portions of the sample, finding an alternative approach to blocking stray light is critical. One possibility to overcome the issue is to increase the efficiency of the optic by resorting to kinoform type X-ray CGHs, with three-dimensional surface-relief structures, which can be fabricated *via* gray-scale ion beam lithography [38,41], stacking [42], multilevel lithography [39,43] or 3D nanoprinting [37]. Another approach could be to encode a secondary phase ramp into the CGH to separate the unwanted 0^{th} order from the actual probe field [24,44] (i.e. use an off-axis GCH). Then the 0th order light can be blocked by an external beamstop. That being said, we have shown (both via experiments and computer simulations) that even when using a binary optic without a beamstop, the technique can succeed in reconstructing the sample exit-wave function.

The discussed CGH generation method can also be used for tailoring the probe wave function with arbitrary complexity. In addition to its uses in X-ray holography, the same approach can be used to generate specialized probes such as vortex beams or for ptychography, coherent diffractive imaging, and other phase-contrast X-ray imaging methods. Furthermore, achieving full control over the phase as well as the amplitude of a structured illumination via a simple monolithic optic has a broad range of applications in acoustic [27] and light-based medical imaging technologies as well as untethered micro-robotic and micromanipulation applications [45–47].

Optics EXPRESS

6. Conclusions

We have applied the DC-GSA algorithm to synthesize efficient X-ray holograms that can project arbitrarily structured illumination with simultaneous phase and amplitude control. With proper design, the optic can concentrate the incident light into an illumination pattern that replaces the physical holography mask in conventional FTH experiments, addressing various limitations of FTH. Through in silico studies as well as an experimental demonstration, we showed that the proposed imaging modality can be used to visualize nano-structures, magnetic textures, and weakly absorbing objects. The method is robust against detector shot noise. The concentrated intensity on the sample plane allows for efficient usage of the coherent flux and positions this method very well for reaping the scientific benefits of current and future high-coherence X-ray sources. The light concentration capability of the diffractive holograms used for StIXH is expected to be a particular advantage for less intense sources, such as high harmonic generation sources where the brightness decreases as the output photon energy increases into the soft X-ray range. Hence, holography experiments using HHG sources will markedly benefit from these proposed condenser optics.

Its single-shot reconstruction capability promises ultra-high time resolution measurements of non-reproducible dynamics using high repetition rate X-ray sources. Furthermore, by decoupling the illumination function from the object, microscopic investigations using X-ray holography will not be limited to preselected regions of interest but rather will be able to explore whole, extended samples such as biological cells or electronic and magnetic devices.

Funding. National Science Foundation (DMR-1231319); Basic Energy Sciences (DE-SC0019126); Deutsche Forschungsgemeinschaft (428809035).

Acknowledgments. K.K. thanks Prof. Gisela Schütz of Max Planck Institute for Intelligent Systems, Prof. Stefan Eisebitt of the Max Born Institute and Dr. Cigdem Ozsoy-Keskinbora of the Harvard University's CIQM for fruitful discussions on off-axis holography and Prof. Robert Westervelt for providing access to CIQM's infrastructure. The authors thank Dr. Eberhard Goering and Mr. Daan B. Boltje of the Max Planck Institute for Intelligent Systems for kindly providing the experimental values of charge and magnetic structure factors for CoFeB and Prof. George Barbastathis for providing the SLM for experiments. K.K. was supported by the German Research Foundation (DFG) under project number 428809035. The MIT based part of this study (part of the computational work, the visible light experiment and data analysis) (A.L., K.K., and R.C.) has been supported by the Department of Energy, Office of Science, Office of Basic Energy Sciences, under Award Number DE-SC0019126. K.K. also acknowledges partial support by the STC Center for Integrated Quantum Materials, NSF Grant No. DMR-1231319.

Disclosures. The authors declare no conflicts of interest.

Data availability. Data underlying the results presented in this paper including the exact multipliers, as well as the synthesis, simulation and analysis scripts are available in Replication Data for: Maskless Fourier Transform Holography, Harvard Dataverse V1, Ref. [48].

Supplemental document. See Supplement 1 for supporting content.

References

1. D. Gabor, *A new microscopic principle*, (Nature Publishing Group, 1948).
2. G. Möllenstedt and H. Düker, "Beobachtungen und Messungen an Biprisma-Interferenzen mit Elektronenwellen," Z. Physik **145**(3), 377–397 (1956).
3. C. Ozsoy-Keskinbora, C. B. Boothroyd, R. E. Dunin-Borkowski, P. A. van Aken, and C. T. Koch, "Hybridization approach to in-line and off-axis (electron) holography for superior resolution and phase sensitivity," Sci. Rep. **4**(1), 7020 (2015).
4. F. Pfeiffer, "X-ray ptychography," Nat. Photonics **12**(1), 9–17 (2018).
5. C. Donnelly, V. Scagnoli, M. Guizar-Sicairos, M. Holler, F. Wilhelm, F. Guillou, A. Rogalev, C. Detlefs, A. Menzel, and J. Raabe, "High-resolution hard x-ray magnetic imaging with dichroic ptychography," Phys. Rev. B **94**(6), 064421 (2016).
6. P. Thibault, M. Dierolf, O. Bunk, A. Menzel, and F. Pfeiffer, "Probe retrieval in ptychographic coherent diffractive imaging," Ultramicroscopy **109**(4), 338–343 (2009).
7. J. M. Rodenburg, "Ptychography and Related Diffractive Imaging Methods," in *Adv. Imaging Electron Phys.*, Hawkes, ed. (Elsevier, 2008), pp. 87-184.

Optics EXPRESS

8. D. A. Shapiro, Y.-S. Yu, T. Tyliszczak, J. Cabana, R. Celestre, W. Chao, K. Kaznatcheev, A. L. D. Kilcoyne, F. Maia, S. Marchesini, Y. S. Meng, T. Warwick, L. L. Yang, and H. A. Padmore, "Chemical composition mapping with nanometre resolution by soft X-ray microscopy," Nat. Photonics **8**(10), 765–769 (2014).
9. X. Shi, N. Burdet, B. Chen, G. Xiong, R. Streubel, R. Harder, and I. K. Robinson, "X-ray ptychography on low-dimensional hard-condensed matter materials," Appl. Phys. Rev. **6**(1), 011306 (2019).
10. Z. Chen, M. Odstrcil, Y. Jiang, Y. Han, M.-H. Chiu, L.-J. Li, and D. A. Muller, "Mixed-state electron ptychography enables sub-angstrom resolution imaging with picometer precision at low dose," Nat. Commun. **11**(1), 2994 (2020).
11. Y. Jiang, Z. Chen, Y. Han, P. Deb, H. Gao, S. Xie, P. Purohit, M. W. Tate, J. Park, S. M. Gruner, V. Elser, and D. A. Muller, "Electron ptychography of 2D materials to deep sub-ångström resolution," Nature **559**(7714), 343–349 (2018).
12. J. R. Fienup, "Phase retrieval algorithms: a personal tour [Invited]," Appl. Opt. **52**(1), 45–56 (2013).
13. J. R. Fienup, "Reconstruction of an object from the modulus of its Fourier transform," Opt. Lett. **3**(1), 27–29 (1978).
14. R. Gradl, M. Dierolf, B. Günther, L. Hehn, W. Möller, D. Kutschke, L. Yang, M. Donnelley, R. Murrie, A. Erl, T. Stoeger, B. Gleich, K. Achterhold, O. Schmid, F. Pfeiffer, and K. S. Morgan, "In vivo Dynamic Phase-Contrast X-ray Imaging using a Compact Light Source," Sci. Rep. **8**(1), 6788 (2018).
15. Z. Najmudin, S. Kneip, M. S. Bloom, S. P. D. Mangles, O. Chekhlov, A. E. Dangor, A. Döpp, K. Ertel, S. J. Hawkes, J. Holloway, C. J. Hooker, J. Jiang, N. C. Lopes, H. Nakamura, P. A. Norreys, P. P. Rajeev, C. Russo, M. J. V. Streeter, D. R. Symes, and M. Wing, "Compact laser accelerators for X-ray phase-contrast imaging," Philosophical Transactions of the Royal Society A: Mathematical Physical and Engineering Sciences **372**, 20130032 (2014).
16. M. P. Olbinado, X. Just, J.-L. Gelet, P. Lhuissier, M. Scheel, P. Vagovic, T. Sato, R. Graceffa, J. Schulz, A. Mancuso, J. Morse, and A. Rack, "MHz frame rate hard X-ray phase-contrast imaging using synchrotron radiation," Opt. Express **25**(12), 13857–13871 (2017).
17. M. Yabashi and H. Tanaka, "The next ten years of X-ray science," Nat Photon **11**(1), 12–14 (2017).
18. S. Eisebitt, J. Luning, W. F. Schlotter, M. Lorgen, O. Hellwig, W. Eberhardt, and J. Stohr, "Lensless imaging of magnetic nanostructures by X-ray spectro-holography," Nature **432**(7019), 885–888 (2004).
19. I. McNulty, J. Kirz, C. Jacobsen, E. H. Anderson, M. R. Howells, and D. P. Kern, "High-Resolution Imaging by Fourier Transform X-ray Holography," Science **256**(5059), 1009–1012 (1992).
20. E. Guehrs, C. M. Güunther, B. Pfau, T. Rander, S. Schaffert, W. F. Schlotter, and S. Eisebitt, "Wavefield back-propagation in high-resolution X-ray holography with a movable field of view," Opt. Express **18**(18), 18922–18931 (2010).
21. P. Hessing, B. Pfau, E. Guehrs, M. Schneider, L. Shemilt, J. Geilhufe, and S. Eisebitt, "Holography-guided ptychography with soft X-rays," Opt. Express **24**(2), 1840–1851 (2016).
22. J. Geilhufe, B. Pfau, M. Schneider, F. Buttner, C. M. Gunther, S. Werner, S. Schaffert, E. Guehrs, S. Frommel, M. Klaui, and S. Eisebitt, "Monolithic focused reference beam X-ray holography," Nat Commun **5**, 3008 (2014).
23. M. Balyan and L. Haroutunyan, "X-ray Fourier transform holography by amplitude-division-type Fresnel zone plate interferometer," J. Synchrotron. Radiat. **25**(1), 241–247 (2018).
24. S. Marchesini and A. Sakdinawat, "Shaping coherent x-rays with binary optics," Opt. Express **27**(2), 907–917 (2019).
25. C. Chang, J. Xia, L. Yang, W. Lei, Z. Yang, and J. Chen, "Speckle-suppressed phase-only holographic three-dimensional display based on double-constraint Gerchberg-Saxton algorithm," Appl. Opt. **54**(23), 6994–7001 (2015).
26. G. Makey, Ö. Yavuz, D. K. Kesim, A. Turnalı, P. Elahi, S. Ilday, O. Tokel, and F. Ö. Ilday, "Breaking crosstalk limits to dynamic holography using orthogonality of high-dimensional random vectors," Nat. Photonics **13**(4), 251–256 (2019).
27. S. Jiménez-Gambín, N. Jiménez, J. M. Benlloch, and F. Camarena, "Holograms to Focus Arbitrary Ultrasonic Fields through the Skull," Phys. Rev. Appl. **12**(1), 014016 (2019).
28. V. Bianco, P. Memmolo, M. Leo, S. Montresor, C. Distante, M. Paturzo, P. Picart, B. Javidi, and P. Ferraro, "Strategies for reducing speckle noise in digital holography," Light: Sci. Appl. **7**(1), 48 (2018).
29. F. Wyrowski and O. Bryngdahl, "Speckle-free reconstruction in digital holography," J. Opt. Soc. Am. A **6**(8), 1171–1174 (1989).
30. G.-Y. Lee, G. Yoon, S.-Y. Lee, H. Yun, J. Cho, K. Lee, H. Kim, J. Rho, and B. Lee, "Complete amplitude and phase control of light using broadband holographic metasurfaces," Nanoscale **10**(9), 4237–4245 (2018).
31. E. Ulusoy, L. Onural, and H. M. Ozaktas, "Full-complex amplitude modulation with binary spatial light modulators," J. Opt. Soc. Am. A **28**(11), 2310–2321 (2011).
32. R. W. Gerchberg and W. O. Saxton, "A Practical Algorithm for the Determination of Phase from Image and Diffraction Plane Pictures," Optik **35**, 237–246 (1972).
33. B. L. Henke, E. M. Gullikson, and J. C. Davis, "X-Ray Interactions: Photoabsorption, Scattering, Transmission, and Reflection at E = 50-30,000 eV, Z = 1-92," At. Data Nucl. Data Tables **54**(2), 181–342 (1993).
34. D. B. Boltje, *Voltage Induced Near Interface Changes of the Magnetocrystalline Anisotropy Energy: A study by X-ray Resonant Techniques in Combination with Conventional Magnetometry* (Universität Stuttgart, 2017).
35. D. G. Voelz, *Computational fourier optics: a MATLAB tutorial* (SPIE, 2011).
36. D. M. Gualtieri, "Magnetic_stripe_domains.jpg" (2011), retrieved 10.02.20, https://commons.wikimedia.org/wiki/File:Magnetic_stripe_domains.jpg.

Optics EXPRESS

37. U. T. Sanli, H. Ceylan, I. Bykova, M. Weigand, M. Sitti, G. Schütz, and K. Keskinbora, "3D Nanoprinted Plastic Kinoform X-Ray Optics," Adv. Mater. **30**(36), 1802503 (2018).
38. K. Keskinbora, C. Grévent, M. Hirscher, M. Weigand, and G. Schütz, "Single-Step 3D Nanofabrication of Kinoform Optics via Gray-Scale Focused Ion Beam Lithography for Efficient X-Ray Focusing," Adv. Opt. Mater. **3**(6), 792–800 (2015).
39. E. D. Fabrizio, F. Romanato, M. Gentili, S. Cabrini, B. Kaulich, J. Susini, and R. Barrett, "High-efficiency multilevel zone plates for keV X-rays," Nature **401**(6756), 895–898 (1999).
40. I. Mohacsi, P. Karvinen, I. Vartiainen, V. A. Guzenko, A. Somogyi, C. M. Kewish, P. Mercere, and C. David, "High-efficiency zone-plate optics for multi-keV X-ray focusing," J. Synchrotron Radiat. **21**(3), 497–501 (2014).
41. K. Keskinbora, U. T. Sanli, C. Grévent, and G. Schütz, "Fabrication and x-ray testing of true kinoform lenses with high efficiencies," (*Proc. SPIE*, 2015), pp. 95920H-95920H-95926.
42. I. Mohacsi, P. Karvinen, I. Vartiainen, A. Diaz, A. Somogyi, C. M. Kewish, P. Mercere, and C. David, "High efficiency x-ray nanofocusing by the blazed stacking of binary zone plates," (*Proc. SPIE* 2013), 88510Z-88510Z-88518.
43. A. Takeuchi, Y. Suzuki, K. Uesugi, I. Okada, and H. Iriguchi, "Performance Test and Evaluation of Multilevel Fresnel Zone Plate with Three-Step Profile Fabricated with Electron-Beam Lithography," Jpn. J. Appl. Phys. **51**, 022502 (2012).
44. H. Wang, Y. Liu, Q. Ruan, H. Liu, R. J. H. Ng, Y. S. Tan, H. Wang, Y. Li, C.-W. Qiu, and J. K. W. Yang, "Off-Axis Holography with Uniform Illumination via 3D Printed Diffractive Optical Elements," Adv. Opt. Mater. **7**(12), 1900068 (2019).
45. A. Aghakhani, O. Yasa, P. Wrede, and M. Sitti, "Acoustically powered surface-slipping mobile microrobots," Proc. Natl. Acad. Sci. **117**(7), 3469–3477 (2020).
46. H. Shahsavan, A. Aghakhani, H. Zeng, Y. Guo, Z. S. Davidson, A. Priimagi, and M. Sitti, "Bioinspired underwater locomotion of light-driven liquid crystal gels," Proc. Natl. Acad. Sci. **117**(10), 5125–5133 (2020).
47. K. Melde, A. G. Mark, T. Qiu, and P. Fischer, "Holograms for acoustics," Nature **537**(7621), 518–522 (2016).
48. K. Keskinbora, "Replication Data for: Maskless Fourier Transform Holography, Harvard Dataverse V1," (Harvard Dataverse, 2021).